The Astrophysical Journal, 967:76 (12pp), 2024 June 1 https://doi.org/10.3847/1538-4357/ad3d49

Pickup Ion Modulation on Plateau-like Turbulence in the Martian Magnetosheath

Hui Li[1,2,3], Wence Jiang[1,2], Zhongwei Yang[1,2], Xiaodong Liu[1,3], Daniel Verscharen[4], and Chi Wang[1,2,3]
[1] State Key Laboratory of Space Weather, National Space Science Center, CAS, Beijing, People's Republic of China; hli@nssc.ac.cn, jiangwence@swl.ac.cn
[2] Key Laboratory of Solar Activity and Space Weather, National Space Science Center, Chinese Academy of Sciences, Beijing, 100190, People's Republic of China
[3] University of Chinese Academy of Sciences, Beijing, People's Republic of China
[4] Mullard Space Science Laboratory, University College London, Dorking RH5 6NT, UK
Received 2024 February 7; revised 2024 March 22; accepted 2024 April 7; published 2024 May 23

Abstract

The distribution of magnetic energy across scales, represented by the turbulence spectrum, provides insights into magnetic field dynamics in astrophysical and space plasma. While the Earth's magnetosheath exhibits a conventional two-slope spectrum, the Martian magnetosheath often displays a prominent plateau-like spectrum. However, the underlying physical mechanism remains unresolved. Based on MAVEN observations, we present appealing evidence of pickup ions (PUIs) modulating the plateau-like spectrum through proton cyclotron waves (PCWs). PCWs, driven by unstable pickup H^+ ion distributions, significantly influence the formation of plateau-like spectra. Both case and statistical studies suggest that the spectral evolution is affected by the relative abundance of pickup O^+ ions. A substantial presence of pickup O^+ ions can suppress PCWs driven by pickup H^+ ions, resulting in a decline in the slope of the plateau spectrum. Particle-in-cell simulations confirm the role of PUI-modulated PCWs in the plateau-range energy injection. Our results provide new insight into the impact of PUIs on magnetic turbulence evolution and associated energy transfer processes in space and astrophysical plasma.

Unified Astronomy Thesaurus concepts: Space plasmas (1544); Planetary magnetospheres (997); Interplanetary turbulence (830)

1. Introduction

Magnetic turbulence within planetary magnetosheaths is a complex phenomenon characterized by nonlinear interactions and stochastic fluctuations. An insightful and commonly employed approach for investigating magnetic turbulence involves the analysis of the power spectral density (PSD) of magnetic field fluctuations as observed by spacecraft. PSDs typically exhibit two broadband power laws in space plasma turbulence, with a spectral break or knee occurring between magnetohydrodynamic (MHD) scales and ion scales (Tu & Marsch 1995; Bruno & Carbone 2013; Verscharen et al. 2019; Sahraoui et al. 2020). In addition to the frequently observed $f^{-5/3}$ scaling, a shallower f^{-1} scaling at MHD scales has been frequently observed within the planetary magnetosheaths of Earth, Saturn, Mercury, Venus, and Mars, where f is the frequency in the spacecraft frame (Czaykowska et al. 2001; Alexandrova 2008; Dwivedi et al. 2015; Hadid et al. 2015; Huang et al. 2017, 2020; Ruhunusiri et al. 2017; Li et al. 2020; Terres & Li 2022).

A recent investigation revealed that the magnetic field spectrum within the Martian magnetosheath frequently exhibits an additional break at MHD scales, presenting a plateau-like spectral feature (Jiang et al. 2023). This plateau-like spectrum is observed in 57% of the spectra and demonstrates a notable correlation with parameters associated with pickup ions (PUIs). However, direct evidence is needed to support the contribution of PUIs to the formation of plateau-like spectra. Numerous studies suggest that the magnetic field spectrum comprises diverse wave modes and structures, including Alfvén waves, fast-mode/slow-mode magnetosonic waves, and coherent structures such as filamentary Alfvén vortices, current sheets, and magnetic holes (Sahraoui et al. 2006; Alexandrova 2008; Vörös et al. 2008; Lion et al. 2016; Huang et al. 2017; Jiang et al. 2022, 2024). The spectral shape and location of the break point suggest the presence of narrowband waves, incoherent and unpolarized fluctuations, and coherent structures with significant amplitudes (Lion et al. 2016). Particularly, coherent waves and structures often span a broad range of frequencies and scales, playing a crucial role in energy transfer and dissipation processes across multiple scales (Osman et al. 2011; Howes 2016; Chasapis et al. 2018; Hou et al. 2023).

In the Martian magnetosheath, neutral particles escaping from the atmosphere undergo ionization and become captured by the electric field of the solar wind, resulting in the formation of PUIs. These PUIs inject substantial free energy into the magnetosheath plasma (Chamberlain 1963; Cravens et al. 1987; Romanelli et al. 2016; Rahmati et al. 2017). In velocity space, the velocity distribution function (VDF) of PUIs often exhibits ring-beam distributions that are susceptible to micro-instabilities, such as the ion cyclotron instability and the mirror-mode instability (Gary & Madland 1988; Neugebauer 1989; Gary 1991; Huddleston et al. 1999; Russell et al. 1999; Matteini et al. 2015). Consequently, the presence of these instabilities gives rise to the emergence of proton cyclotron waves (PCWs) and other modes within the Martian magnetosheath (Brain 2002; Romanelli et al. 2013; Delva et al. 2015; Harada et al. 2019). Hybrid kinetic simulations have shown that up to 25% of the energy carried by newly formed ions is lost to wave growth through these instabilities (Cowee et al. 2007, 2008; Cowee & Gary 2012). The generated PCWs exhibit left-hand polarization and propagate almost along the background magnetic field. Furthermore, heavy PUI species, such as pickup O^+ ions, are frequently observed within the Martian magnetosheath, originating from the loss of the Martian atmosphere (Jakosky et al. 1994, 2015a; Chassefière

& Leblanc 2004; Dong et al. 2015; Rahmati et al. 2015, 2017). These heavy ions have the potential to alter wave properties, including the introduction of a damping effect on wave instability such as PCW instability (Gary 1991). In this study, we aim to test the hypothesis that the presence of a significant component of pickup O^+ ions suppresses the generation of PCWs by the unstable pickup H^+ ions, thereby affecting the plateau-like feature observed in the turbulent power spectrum within the Martian magnetosheath.

It is conceivable that the injection of energy directly alters the characteristics of the background turbulence, such as the energy cascade rate, within a compressible plasma with highly anisotropic temperatures of particles. Recent investigations have reported similar alterations in the upstream and downstream regions of planetary bow shocks (Hadid et al. 2018; Andrés et al. 2019, 2020). A one-dimensional hybrid simulation (Cowee et al. 2008) suggests that the injection of wave energy in the form of PCWs gradually transfers inversely to larger wavelengths over time, particularly under conditions of strong injection. However, the interplay between kinetic-scale instabilities and the background turbulence remains largely unexplored. The impact of kinetic instabilities on magnetosheath turbulence, including its spectral scaling and energy cascade rates, presents significant challenges in understanding planetary plasma environments.

In this investigation, we propose that the spectral shape variation and associated fluctuations are modulated by the ring-beam instability of PUIs observed within the Martian magnetosheath. By combining a case analysis from MAVEN data and corresponding particle-in-cell simulations, our study provides compelling evidence of microinstabilities originating from PUIs and the subsequent emergence of energy injections of short-wavelength fluctuations, thereby accounting for the distinct plateau-like spectra observed.

2. Observations

2.1. Plateau-like Spectra in the Martian Magnetosheath

Figure 1 shows an event with plateau-like magnetic field spectra observed on the flank of the Martian magnetosheath by the MAVEN spacecraft. This event is from UT 11:50:00 to 13:20:00 on 2016 May 9, characterized by a plateau-like spectrum shown in Figure 1(g). The top three panels present the magnetic field fluctuations (B), the ion number density (n), and the velocity (V). These measurements in the Mars Solar Orbital (MSO) coordinate system were obtained from the Solar Wind Ion Analyzer (SWIA; Halekas et al. 2015) and the Magnetometer (Connerney et al. 2015) instruments on board the MAVEN spacecraft (Jakosky et al. 2015b). Figures 1(d) and (e) show the wave normal angle (θ_{kB}) and the ellipticity of the magnetic field fluctuations obtained by the singular value decomposition (SVD) method (Santolík et al. 2003). Figure 1(f) gives the wavelet spectrum of the magnetic field fluctuations divided by $f^{-5/3}$.

As shown in Figure 1(h), the spacecraft during this interval predominantly resides on the far flank of the Martian magnetosheath, away from both the bow shock and the magnetic pileup boundary (MPB; Trotignon et al. 2006). This event is characterized by a consistent plasma flow with an average bulk speed of 283 km s^{-1}. The average ion β is 0.7, and the average turbulent Mach number $M_{\mathrm{turb}} = \delta v / C_{\mathrm{s}}$ is 0.18, where δv represents the velocity fluctuation and C_{s} signifies the sound speed. This indicates that the magnetosheath plasma in this interval exhibits lower degrees of fluctuation in magnetic field and density and a steady flow condition compared to magnetosheath regions near the bow shock (not shown here).

Figure 1(g) displays the omnidirectional PSD of the magnetic field fluctuations by applying Welch's method and conducting a fast Fourier transform on the magnetic field data (Li et al. 2020). The magnetic field data have a time resolution of 1/32 s, resulting in a Nyquist frequency of 16 Hz. Notably, distinct power-law behaviors are observed at different frequencies/scales in the spectrum, prompting us to utilize a linear fitting method in double-logarithmic space to determine the spectral indices. The colored lines represent the power-law spectra obtained through our linear fitting procedure. Solid vertical lines correspond to Doppler-shifted frequencies $f_{\rho \mathrm{i}} = v_{\mathrm{sw}}/2\pi\rho_{\mathrm{i}}$ (in red) and $f_{\mathrm{di}} v_{\mathrm{sw}}/2\pi d_{\mathrm{i}}$ (in blue), where $\rho_{\mathrm{i}} = v_{\mathrm{th}\perp}/\Omega_{\mathrm{cp}}$ denotes the proton gyroradius, Ω_{cp} represents the proton gyrofrequency, $v_{\mathrm{th}\perp}$ is the thermal speed of plasma protons, $d_{\mathrm{i}} = v_{\mathrm{A}}/\Omega_{\mathrm{cp}}$ is the proton inertial length, and v_{A} is the Alfvén speed.

The magnetic field spectrum exhibits a spectral break near 0.2–0.3 Hz. A distinctive plateau-like transition range is observed, as illustrated in Figure 1(g). When the frequency is less than 10^{-2} Hz, the PSD follows a power law of $f^{-1.93}$. When the frequency ranges from 10^{-2} Hz to 0.2 Hz, the PSD exhibits a flatter power law of $f^{-0.31}$. When the frequency is greater than 0.2 Hz, at kinetic scales, the PSD displays a steeper power law of $f^{-3.13}$, which deviates from the typical $f^{-2.8}$ scaling observed in Earth's magnetosheath (Li et al. 2020). Our previous study has extensively examined such a plateau-like feature (Jiang et al. 2023). The occurrence rate of plateau-like characteristics shows a comprehensive statistical correlation with PUI-related parameters, such as the pickup angle in velocity space and the ion β. However, it is still unclear on its variability and related physical mechanisms.

To gain insight into the nature of the magnetic field fluctuations observed, we employ the SVD method to extract wave properties, such as the wave normal angle (θ_{kB}) and the ellipticity, as shown in Figures 1(d) and (e). In each panel, the black lines represent the Doppler-shifted frequency (Jian et al. 2010),

$$f_{\mathrm{ci,sc}} = f_{\mathrm{ci,sw}} (1 + M_{\mathrm{A}} \hat{\boldsymbol{k}} \cdot \hat{\boldsymbol{v}}_{\mathrm{i}}), \tag{1}$$

where $f_{\mathrm{ci,sw}}$ denotes the proton cyclotron frequency, M_{A} represents the Alfvén Mach number, $\hat{\boldsymbol{k}}$ is the unit wavevector, and $\hat{\boldsymbol{v}}_{\mathrm{i}}$ is the unit vector of ion bulk velocity. We observe the presence of continuous PCWs accompanied by substantial perpendicular magnetic field fluctuations ($(\delta B_{\perp}/\delta B_{\parallel})^2 \approx 10$). These PCWs exhibit a small wave normal angle ($\theta_{\mathrm{kB}} \approx 20$) and an ellipticity close to -1 around $f \approx f_{\mathrm{ci}}$. By examining the compensated PSDs shown in Figure 1(f), we find that PCWs coherently introduce significant and broadband magnetic field fluctuations onto the background turbulent fluctuations. This could lead to the formation of a plateau-like feature in the PSD shown in Figure 1(g), resulting in two spectral breaks. However, we notice that the compensated spectrum shown in Figure 1(f) reveals an interesting modulation on the magnetic field spectral shape from 12:00:00 to 12:30:00 UT. The amplitudes of low-frequency magnetic field fluctuations are enhanced, and the signals of PCWs seem to be weakened

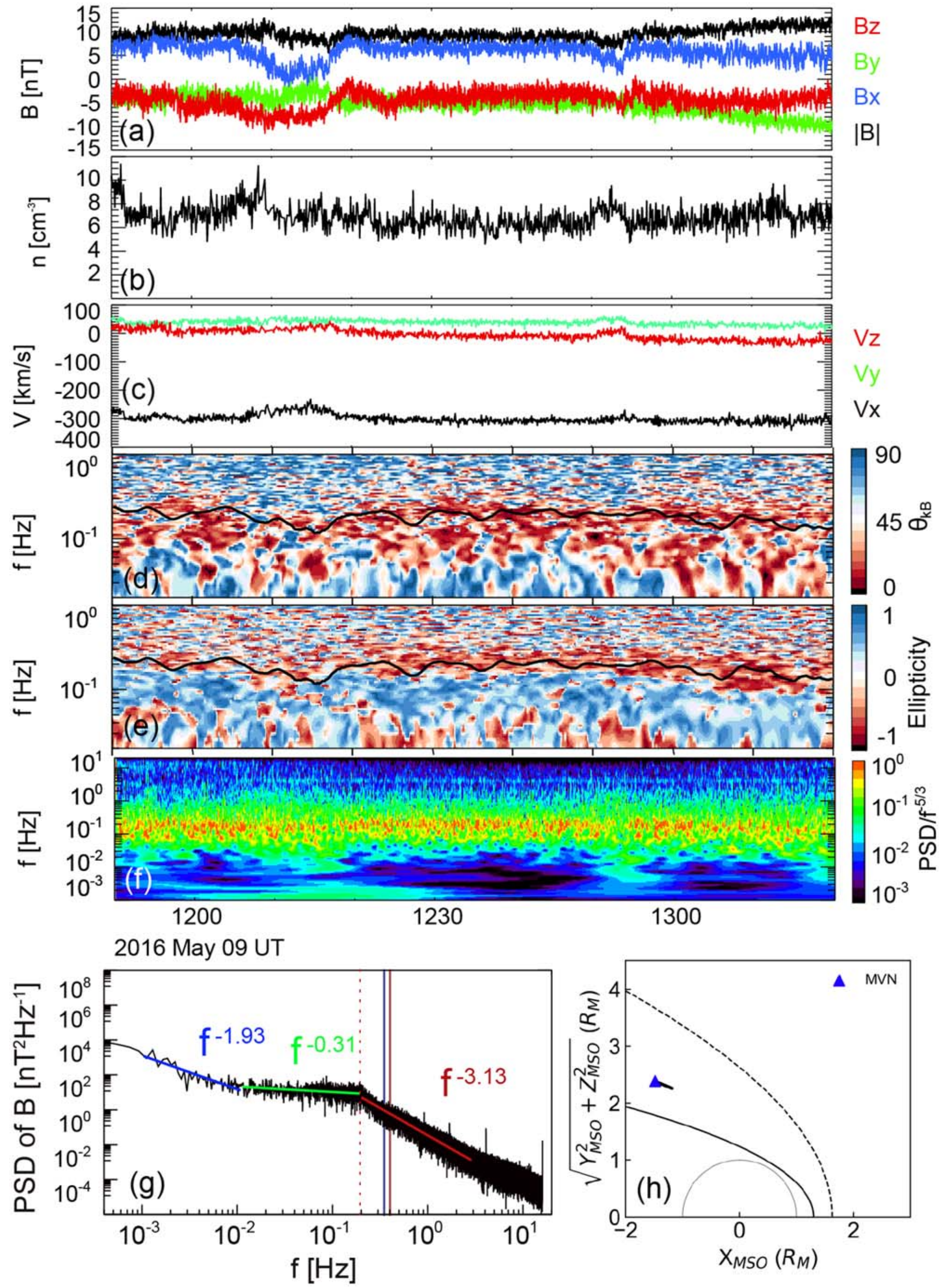

Figure 1. A plateau-like magnetic field spectrum case was observed on the flank of the Martian magnetosheath. From top to bottom, the panels display the magnetic field, the ion number density, the bulk velocity, the propagation angle of magnetic field fluctuations, the ellipticity calculated using the SVD method, the wavelet spectrum of the magnetic field fluctuations divided by $f^{-5/3}$, the omnidirectional PSDs of the magnetic field fluctuations, and the corresponding spacecraft trajectory. All data are presented in the MSO coordinate system. The black lines in panels (d) and (e) represent half of the Doppler-shifted proton cyclotron frequencies in the spacecraft frame calculated from Equation (1). The solid vertical lines in panel (g) indicate the Doppler-shifted proton gyroscale frequency (red) and the proton inertial-length frequency (blue). The red dotted vertical line corresponds to the spectral break frequency around the ion scales. The black dashed and solid lines in panel (h) show the nominal position of the bow shock and the MPB.

during this subinterval when significant oxygen ions are present, as we will show next.

2.2. Pickup O^+ Modulation of Plateau-like Spectra

Figures 2(a) and (b) show the spectrograms of ion differential energy flux from SWIA and the ion mass-energy flux retrieved from STATIC C6 data. In Figure 2(a), the black and cyan colored lines represent the maximum pickup energy ($E_{\mathrm{j,max}}$) for pickup H^+ or O^+ ions, given by the equation

$$E_{\mathrm{j,max}} = 2m_{\mathrm{j}}v_{\mathrm{sw}}^2\sin^2\alpha_{\mathrm{BV}}, \tag{2}$$

where m_{j} denotes the mass of ion species j, v_{sw} represents the bulk speed of the solar wind, and α_{BV} is the angle between the proton bulk velocity and the magnetic field. Equation (2) illustrates that PUIs with different masses have distinct maximum pickup energies.

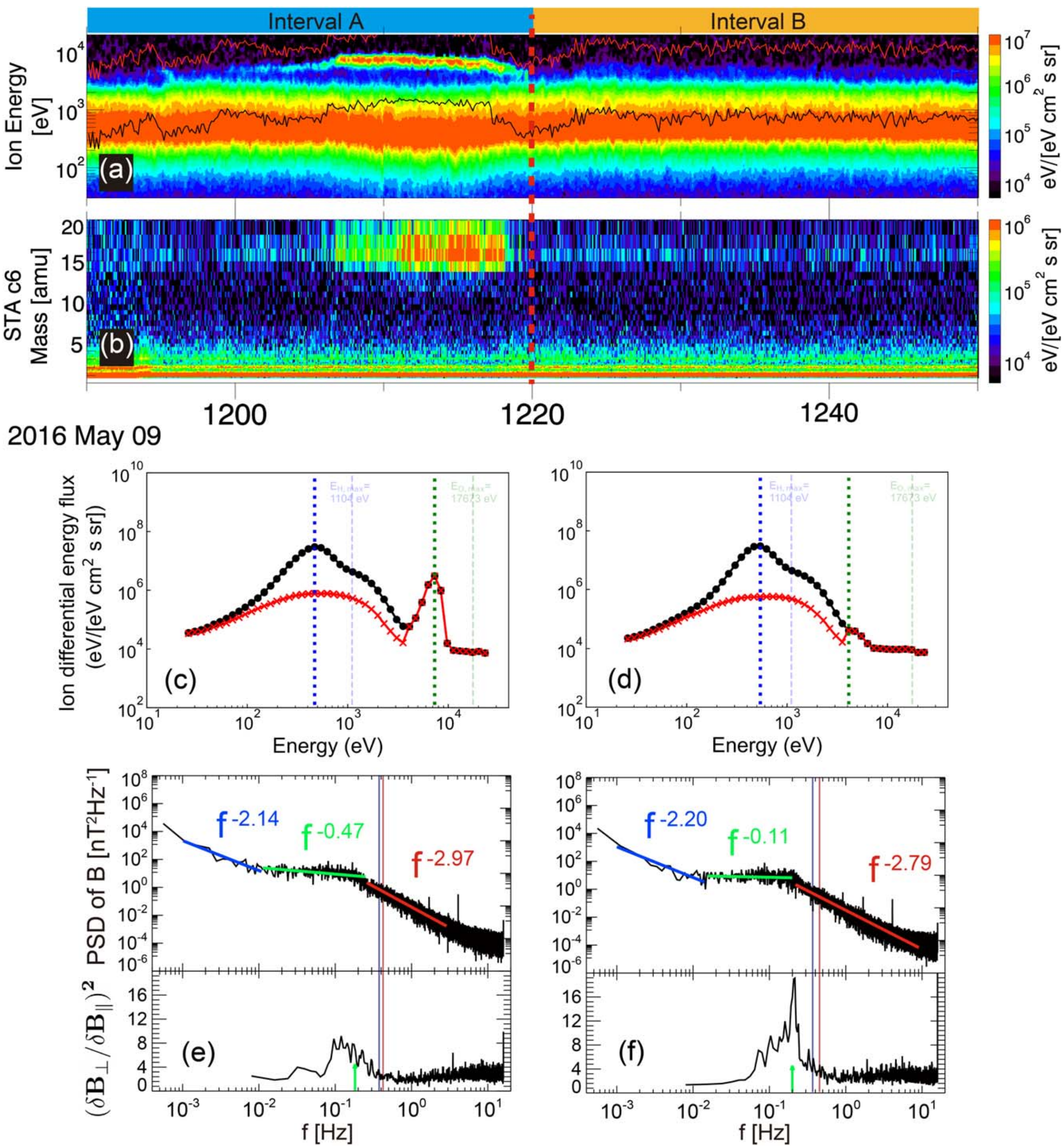

Figure 2. Observation of PUIs and their influence on the spectral shape of the magnetic field for case B. (a) The spectrogram of the ion differential energy flux obtained from SWIA. The colored lines, representing the maximum pickup energy for pickup H^+ (black) and pickup O^+ (red), are calculated using Equation (2). (b) Spectrogram of the ion mass differential energy flux derived from STATIC C6 data. (c) and (d) are the time-averaged one-dimensional ion differential energy flux as a function of ion energy for intervals 1 and 2. The black circles represent the original fluxes of all SWIA look directions. The red crosses represent fluxes of SWIA look directions without significant contamination from solar wind ions (see the Appendix). The vertical dotted lines indicate the energies corresponding to the enhanced flux of the pickup H^+ (blue) and the pickup O^+ (green). (e) and (f) PSDs and the ratio $(\delta B_\perp/\delta B_\parallel)^2$ of magnetic field fluctuations.

The observed enhancement in ion flux around 7000 eV, measured by SWIA from 12:07:00 to 12:17:00 UT, is consistent with the estimated maximum energy ($\leqslant E_{\mathrm{O,max}}$) of pickup O^+ ions. Furthermore, the STATIC data reveal an increase in ion flux at a mass of 16 amu, providing additional evidence for the significant presence of pickup O^+ ions in case A. In contrast, there is a notable decrease in the observed pickup O^+ ions in case B. However, distinguishing pickup H^+ ions from the background solar wind protons proves challenging because of their identical masses. To address this challenge, we first employ time averaging to obtain the one-dimensional ion differential energy flux from SWIA as a function of ion energy for two intervals: interval 1 (from 11:50:00 to 12:20:00 UT) and interval 2 (from 12:20:00 UT to 12:50:00 UT). According to Equation (2), when the angle α_{BV} is 90°, the maximum energy of locally generated pickup H^+ ions should be 4 times the kinetic energy of the solar wind bulk velocity (i.e., the central peaks in Figures 2(c) and (d)).

To evaluate the relative ratios among different ion populations, we first extract partial ion differential energy flux (red crosses in Figures 2(c) and (d)) by ruling out the contamination from solar wind ions within 16 fixed look directions of SWIA that point toward the solar wind bulk flow (for details, see Figure 6). Checking different look directions has been proven useful in a previous study since PUIs are usually from different look directions of SWIA than solar wind ions (Rahmati et al. 2017). Then, we compute the ratios of one-dimensional ion differential energy flux at corresponding energies of ions with different origins such as the pickup H^+ and O^+ and the solar wind H^+. Accelerated PUIs with different masses are usually well separated from the bulk solar wind ions in energy according to Equation (2), as shown in Figures 2(c) and (d). We specifically highlight the maximum fluxes of bulk solar wind ions, pickup H^+ ions (indicated by the blue vertical line), and pickup O^+ ions (indicated by the green vertical line). We also show the corresponding maximum pickup energies $E_{\mathrm{H,max}}$ and $E_{\mathrm{O,max}}$ for pickup H^+ and O^+ in Figures 2(c) and (d). Because the ions originating from the solar wind in the magnetosheath are more thermally distributed than those in the upstream solar wind, we observed that the majority of pickup H^+ ions can be extracted from thermal H^+ by excluding data from look directions with azimuths/anodes 14–16 and elevations 1–4, where the thermal ions tend to concentrate. We use the theoretical maximum pickup proton energy $E_{\mathrm{H,max}}$ and its corresponding partial differential energy flux as the approximate flux of the pickup H^+ ions. Therefore, we directly approximate the relative density ratios between PUIs and solar wind protons from their one-dimensional differential energy fluxes. For intervals 1 and 2, we find the average density ratios between pickup H^+ ions and the solar wind H^+ ions $n_{\mathrm{PUI,H}}/n_{\mathrm{SW,H}} = 0.08$, as well as between pickup O^+ ions and pickup H^+ ions $n_{\mathrm{PUI,O}}/n_{\mathrm{SW,H}} = 0.58$ and 0.01. Our observations indicate that the density ratio between pickup H^+ ions and solar wind H^+ ions remains nearly constant (approximately 0.08) for both intervals. However, the density ratio between pickup O^+ ions and pickup H^+ ions is significantly higher in interval 1 (0.58) than in interval 2 (0.01). Since the SWIA does not discriminate different ion masses, converting the differential energy flux ratio to the number density ratio between O^+ and H^+, which have different masses, requires a multiplication factor of $1/\sqrt{m_{\mathrm{O}}/m_{\mathrm{H}}} = 1/4$. This estimation has been confirmed by calculating the densities of the three ion populations using a partial moment method for different look directions and energies (see Figure 7).

Figure 2 provides insights into the observed enhancement of pickup O^+ flux, which is exclusively present in interval 1. However, PCW activity is evident in both intervals, as depicted in Figure 1(d). We compute the PSDs of the magnetic field for the two intervals, with the same duration, ranging from 11:50:00 to 12:20:00 UT (interval 1) and from 12:20:00 to 12:50:00 UT (interval 2). Figures 2(e) and (f) illustrate the PSDs, the results of the power-law fitting, and the average ratio $(\delta B_{\perp}/\delta B_{\parallel})^2$ for intervals 1 and 2. In both intervals, the computed magnetic field spectra exhibit a plateau-like shape. However, interval 2 demonstrates a higher value of $(\delta B_{\perp}/\delta B_{\parallel})^2$ (approximately 18) at the Doppler-shifted proton cyclotron frequency (indicated by the green arrow) compared to interval 1 (approximately 8). As quasi-parallel propagating PCWs predominantly manifest fluctuating energy in the transverse components of the magnetic field, this finding suggests that the intensity of the PCWs in interval 2 surpasses that of interval 1. Additionally, we observe that the power spectral index in the plateau-like range during interval 2 is −0.11, which is higher than during interval 1, −0.47. No significant distinctions are discerned in the spectral shape at sub-ion scales or frequencies below 10^{-2} Hz. Consequently, we propose that the spectral index of the plateau-like spectrum varies with PCW intensity.

Figures 3(a) and (b) showcase the ion VDFs in the $(v_{\parallel}, v_{\perp})$ plane of the plasma rest frame, where $v_{\parallel}$ and $v_{\perp}$ denote the parallel and perpendicular velocity components relative to the direction of the background magnetic field. The isocontours of the ion VDFs are displayed, with color indicating the phase-space density of the ions. To obtain the ion VDFs in the plasma rest frame, we first subtract the original ion VDFs in the SWIA instrument frame with the integrated ion bulk velocity every 4 s. Next, we convert the ion VDFs from spherical coordinates to cylindrical magnetic-field-aligned coordinates. Finally, we bin the obtained ion VDFs onto the (α, E) plane with a fixed number of pitch angles and logarithmic energy steps, where α and E denote the pitch angle and the energy of the ions. It should be noted that due to the limited field of view of the SWIA instrument, there are some regions with missing data. The ion VDFs presented in Figures 3(a) and (b) correspond to the oxygen-rich interval (12:08:00–12:18:00) and the oxygen-poor interval (12:29:59–12:40:03), respectively. Dashed semicircles are utilized to represent the maximum velocities of pickup H^+ ions ($E_{\mathrm{H,max}}$; red) determined by Equation (2). According to Equation (2), we anticipate that heavy ions such as O^+ possess higher energies compared to solar wind protons and pickup H^+ ions. Indeed, Figure 3(a) exhibits a distinct ringlike population in the VDF, characterized by energies significantly exceeding the core thermal energy ($\leqslant$100 eV) but remaining below $E_{\mathrm{O,max}}$ ($\geqslant$10,000 eV).

Conversely, no similar pattern is discernible in Figure 3(b). We attribute this ringlike distribution to the pickup O^+ ions, which appear to have transformed into a bispherical shell distribution, potentially due to wave–particle interactions (Matteini et al. 2015). In Figure 3(a), we identify that the majority of the pickup oxygen population, extending beyond the ion core population, is concentrated at pitch angles near 100°. In velocity space, we also readily identify the pickup H^+ population near $E_{\mathrm{H,max}}$ (red semicircle), which manifests as a distinct bulge protruding from the core H^+ population with pitch angles ranging from 30° to 90° (between the first two black dotted lines in Figure 3(a)). To further extract the key parameters of the VDFs of different ion populations, we employ a VDF fitting model based on the Markov Chain Monte Carlo algorithm for the VDF data. Therefore, we determine that the pitch angle of pickup H^+ ions, $\alpha_{\mathrm{PUI,H}}$, is approximately 30° in Figure 3(b), while in Figure 3(a), $\alpha_{\mathrm{PUI,H}}$ is approximately 62°.9. Our fitting approach suggests that the central pitch angle of the pickup O^+ ions, $\alpha_{\mathrm{PUI,O}}$, is approximately 108°.5 as shown in Figure 3(a). We also determine the central drift velocities of two distinct PUI populations as $u_{\mathrm{PUI,\ H}}/v_{\mathrm{A}} = 4$ and $u_{\mathrm{PUI,\ O}}/v_{\mathrm{A}} = 2.25$, where $v_{\mathrm{A}} \approx 100\ \mathrm{km\ s^{-1}}$ is the average Alfvén speed. We note that the SWIA does not discriminate different ion masses; thus, the drift velocity of pickup O^+ should be smaller by a factor of $\sqrt{m_{\mathrm{O}}/m_{\mathrm{H}}} = 4$.

In concurrence with the time intervals employed for retrieving the ion VDFs, Figures 3(c) and (d) showcase the bandpass-filtered perpendicular magnetic field fluctuations within the frequency range of 0.20–0.21 Hz, approximately

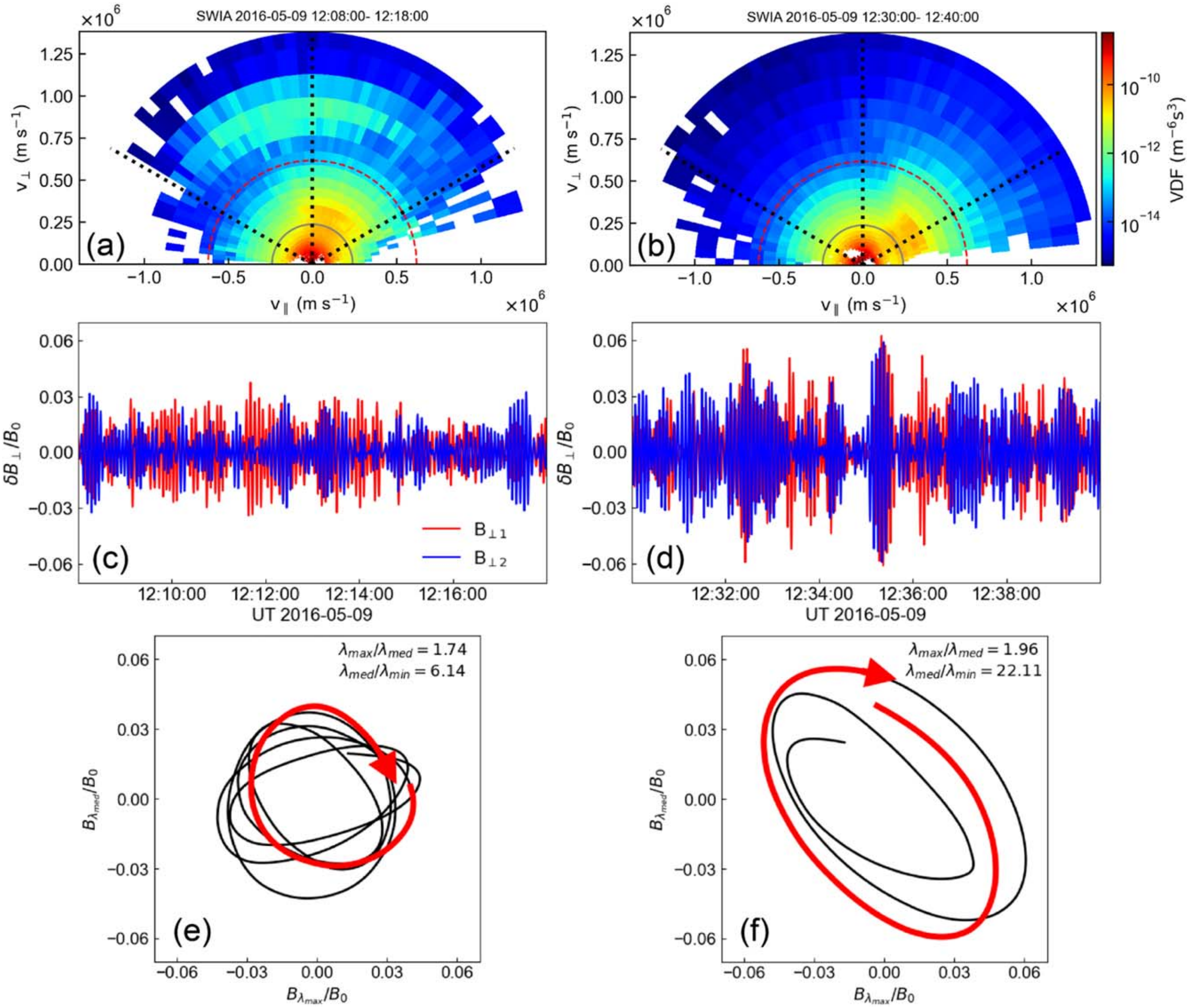

Figure 3. Evidence of pickup H^+ and O^+ populations with ring-beam configurations in velocity space and their association with magnetic field oscillations of PCWs. (a) and (b) are the time-averaged ion VDFs during the oxygen-rich interval (12:08:00–12:18:00) and the oxygen-poor interval (12:29:59–12:40:03), respectively. The dashed semicircles represent the maximum velocities of pickup H^+ (red), calculated using Equation (2). The black dotted lines correspond to pitch angles of 30°, 90°, and 150°. (c) and (d) are the bandpassed magnetic field fluctuations in the plane perpendicular to the background field direction within the frequency band of 0.20–0.21 Hz. The red and blue lines represent the time series of the two orthogonal components, normalized to the background magnetic field B_0. (e) and (f) The hodograms of the magnetic field fluctuations on their maximum and intermediate variance plane ($B_{\lambda_{\max}}$, $B_{\lambda_{\rm med}}$) within the frequency band of 0.20–0.21 Hz computed from the MVA technique. The red arrows show the rotation direction of magnetic field fluctuations.

corresponding to $f_{\rm ci,sc}$. The red and blue curves represent the components $\delta B_{\perp 1}$ and $\delta B_{\perp 2}$ of the magnetic field on a plane perpendicular to the average direction of the background magnetic field, respectively. To provide additional information on the polarization of the waves, we employ a minimum variance analysis (MVA) technique to the bandpass-filtered magnetic field fluctuations of two intervals (Sonnerup & Scheible 1998). We show the hodograms of the analyzed magnetic field perturbations on the maximum and intermediate variance plane ($B_{\lambda_{\max}}$, $B_{\lambda_{\rm med}}$). The red arrows indicate the direction of rotation of the fluctuating magnetic field in the ($B_{\lambda_{\max}}$, $B_{\lambda_{\rm med}}$) plane. During UT 12:10:00–12:11:00, the ratio between maximum (intermediate) and intermediate (minimum) eigenvalues is 1.74 (6.14). During UT 12:31:20–12:31:35, the ratio between the maximum (intermediate) and intermediate (minimum) eigenvalues is 1.96 (22.11). The angle between the average magnetic field direction and the normal direction derived from the MVA technique is 67°.8 and 71°.5, respectively. These results suggest that the PCWs observed during the two intervals are elliptically left-handed polarized and obliquely propagating. The average amplitude of the perpendicular magnetic field fluctuations is 0.13 nT (equivalent to 0.015 B_0) for interval 1, while it increases to 0.20 nT (equivalent to 0.022 B_0) for interval 2. Notably, the intensity of the PCWs appears to be lower when the relative ratio between pickup O^+ and pickup H^+ is higher. This finding supports our hypothesis that pickup O^+ may suppress the generation of PCWs by pickup H^+.

2.3. Statistical Results

Based on the event list covering 4 yr (2015–2019) of MAVEN observations in the Martian magnetosheath given by Jiang et al. (2023), we conduct a statistical analysis of the relationship between density ratios of pickup oxygen/hydrogen ions ($n_{\rm PUI,O}/n_{\rm PUI,H}$) and the average transverse ratio of

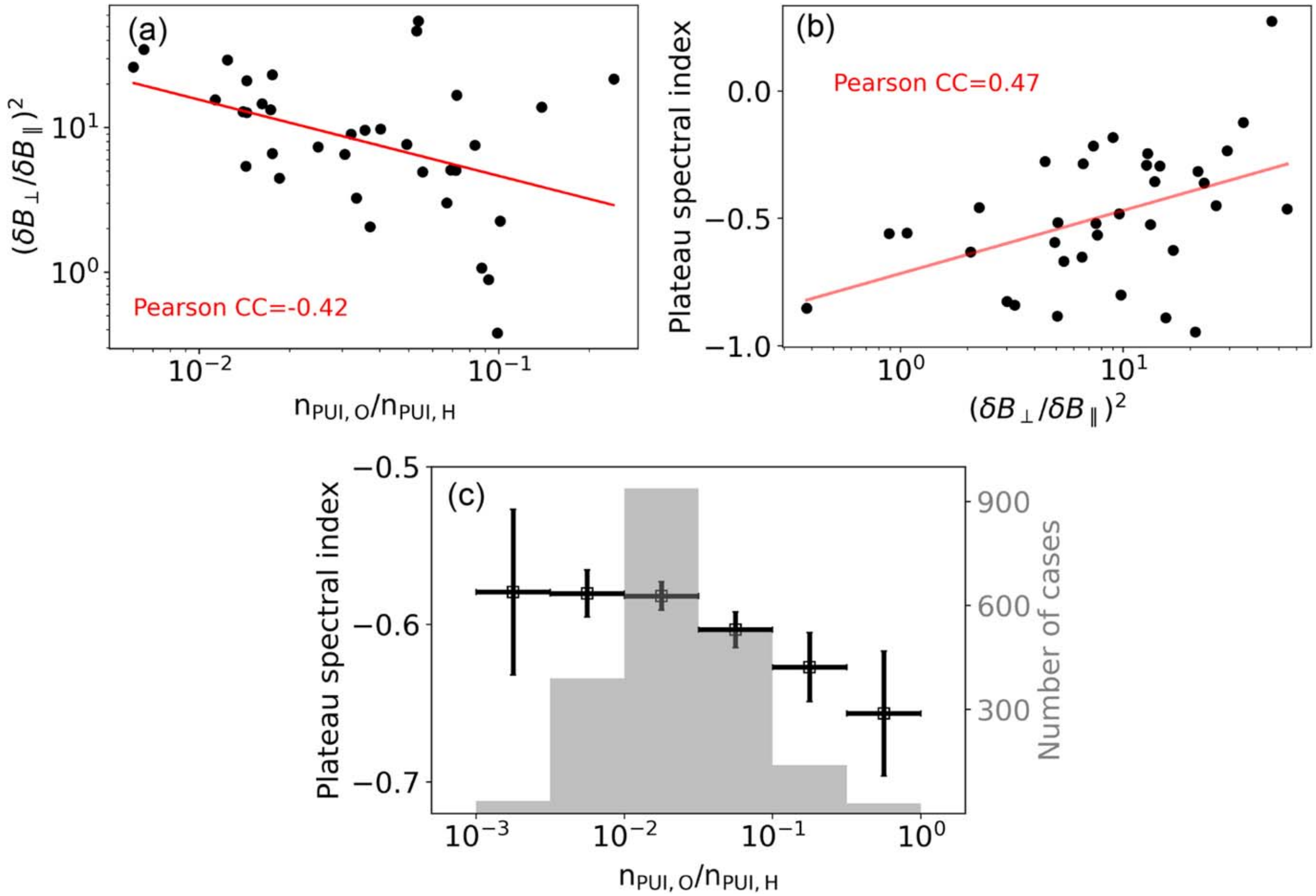

Figure 4. Statistical results of the average transverse ratio of magnetic field fluctuations $(\delta B_\perp/\delta B_\parallel)^2$ near the proton cyclotron frequency, the relative PUI ratio $n_{\rm PUI,O}/n_{\rm PUI,H}$, and the plateau spectral index of the magnetic field PSD. The red lines in (a) and (b) represent the linear fitting lines. The error bars in (c) represent the standard error of the mean value (vertical) and the range of $n_{\rm PUI,O}/n_{\rm PUI,H}$ to calculate the mean value (horizontal).

Table 1
Parameters of Simulation Setup Based on Key Parameters Extracted from MAVEN Observations of Interval 1 (11:50:00–12:20:00 UT) and Interval 2 (12:20:00–12:50:00 UT)

Runs	$n_{\rm PUI,O}/n_{\rm PUI,H}$	$n_{\rm PUI,H}/n_{\rm SW,H}$	$u_{\rm PUI,H}/v_{\rm A}$	$u_{\rm PUI,O}/v_{\rm A}$	$\alpha_{\rm PUI,H}$	$\alpha_{\rm PUI,O}$
1	0.58	0.08	4	2.25	30°	108°.5
2	0.01	0.08	4	2.25	30°	108°.5

magnetic field fluctuations $(\delta B_\perp/\delta B_\parallel)^2$ near the proton cyclotron frequency, as well as the plateau spectral index of the magnetic field PSD. Similar to our case study, we used a comparable method to extract both pickup oxygen and hydrogen ions and obtain their relative ratio $n_{\rm PUI,O}/n_{\rm PUI,H}$.

We analyze 36 cases with significant PCW signatures (i.e., $\theta_{kB} < 30$ and ellipticity < -0.5), as well as plateau-like magnetic field spectral characteristics in the Martian magnetosheath. As shown in Figure 4(a), the transverse ratio of magnetic field fluctuations $(\delta B_\perp/\delta B_\parallel)^2$ is negatively correlated with the relative ratio of pickup oxygen and hydrogen $n_{\rm PUI,O}/n_{\rm PUI,H}$, with a Pearson correlation coefficient of -0.42 and a p-value of 0.011. At the same time, as shown in Figure 4(b), it is positively correlated with the plateau spectral index of the magnetic field PSD, with a Pearson correlation coefficient of 0.47 and a p-value of 0.004.

Furthermore, we conduct a statistical survey of 2060 magnetosheath cases resembling a plateau-like spectral feature in the magnetic field PSD. Figure 4(c) shows that the average plateau spectral indices vary with the relative ratio $n_{\rm PUI,O}/n_{\rm PUI,H}$. The average plateau spectral indices decrease from -0.58 to -0.67 as the $n_{\rm PUI,O}/n_{\rm PUI,H}$ increases from 0.02 to 0.56. This statistical result aligns well with the conclusion of the previous case study. Therefore, we suggest that the increase of heavy oxygen ion abundance suppresses the amplitude of PCWs, leading to the decrease in the plateau spectral index of the magnetic field PSD.

3. Particle-in-cell Simulations

To examine the influence of pickup O^+ ions on the generation of PCWs, we conduct 1D-3V particle-in-cell simulations initialized with the observational parameters listed in Table 1. Figure 5 presents the results of two simulation runs, each employing different density ratios of pickup O^+ to pickup H^+ ions according to our observations. In Figures 5(a) and (c), we show two intermediate snapshots at $t = 100\Omega_{\rm ci}^{-1}$ of the time

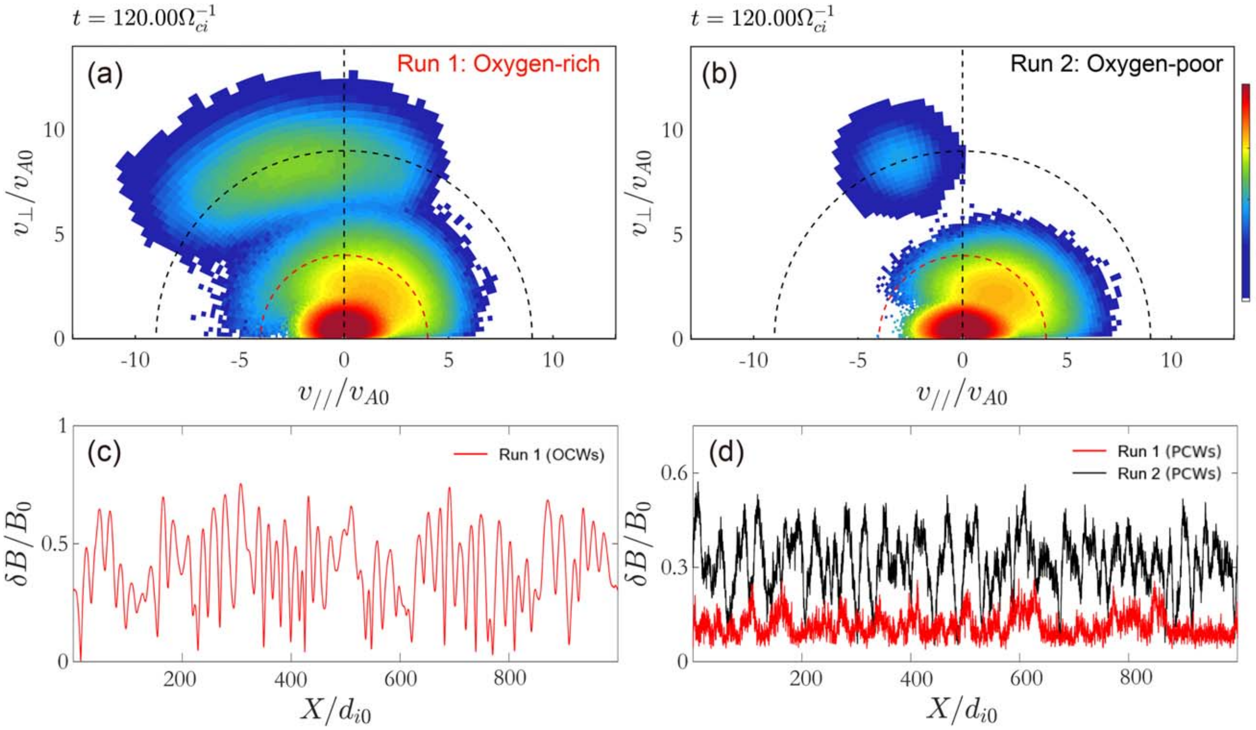

Figure 5. Particle-in-cell simulation results of run 1 and run 2. (a) and (b) are the ion VDFs at $t = 120\Omega_{\rm ci}^{-1}$ evolved from the initial conditions characterized in Table 1. The color indicates the normalized phase-space density of the ions. (c) and (d) are the perpendicular magnetic field fluctuations as a function of X at $t = 120\Omega_{\rm ci}^{-1}$. The black and red lines in (d) represent the PCWs filtered out near the local proton cyclotron frequency in both runs. The red line in (c) represents the OCWs filtered near the local cyclotron frequency of O^+ in run 1.

evolution of ion VDFs from run 1 and run 2 initiated by the parameters listed in Table 1, where $\Omega_{\rm ci}^{-1}$ denotes the cyclotron frequency of the protons. The solar wind and the O^+ ions are initialized with bi-Maxwellian distribution functions in velocity space. The background magnetic field is aligned with the X-axis. We use key parameters extracted from Figures 3(a) and (b) to approximate the observational velocity-space characteristics of different ions. For pickup O^+ ions, they are initiated with parallel and perpendicular drift velocities $(u_\parallel,\ u_\perp) = (-0.71,\ 2.13)v_{\rm A}$ or, equivalently, the velocity drift and pitch-angle shift $(u_{\rm PUI,O}/v_{\rm A}) = (2.25v_{\rm A},\ 108^\circ\!.5)$. For pickup H^+ ions, they possess $(u_\parallel,\ u_\perp) = (3.46,\ 2.0)v_{\rm A}$ or, equivalently, $(u_{\rm PUI,H}/v_{\rm A},\ \alpha) = (4v_{\rm A},\ 30^\circ)$. For both simulation runs, we set the pitch angle of pickup H^+ ions to 30° for self-consistency. For run 1 (run 2), the relative densities between the PUIs are $n_{\rm PUI,O}/n_{\rm SW,H} = 0.58(0.01)$ (see Table 1).

By examining the time and spatial evolution of perpendicular magnetic field fluctuations for run 1 and run 2, we find that the PCWs are first excited for both runs. At $t \approx 70\Omega_{\rm ci}^{-1}$, large-amplitude oxygen cyclotron waves (OCWs) are starting to inject due to the great density ratio between the PUIs, $n_{\rm PUI,O}/n_{\rm PUI,H} = 0.58$, in run 1, whereas in run 2, no OCWs and PCWs are persistently present. By comparing the VDFs of both runs at $t = 120\Omega_{\rm ci}^{-1}$, we find that the pickup H^+ are less pitch-angle-scattered in run 2 (oxygen-poor) than in run 1 (oxygen-rich) as shown in Figures 5(a) and (b). However, at $t = 120\Omega_{\rm ci}^{-1}$, the pitch-angle-scattered pickup H^+ seems to be centered at a pitch angle of around 60°, which is very similar to our observation in Figure 3(a). Therefore, we suggest that the pickup oxygen and hydrogen ions in the VDF shown in Figure 3(a) are under significant action of pitch-angle scattering.

By filtering out fluctuations near the oxygen cyclotron frequency, we find that the power of injected PCWs generated by pickup H^+ is higher in run 2 (see Figure 5(d)). The presence of pickup O^+ seems to lead to the suppression of PCWs. The unstable wavenumber range of PCWs is reduced when pickup O^+ is included, indicating that pickup H^+ can no longer drive PCWs over the same wavenumber range. We find that the VDF of pickup H^+ shown in Figure 5(a) is more isotropic and pitch-angle-scattered than in Figure 5(c), meaning that the OCWs could also have scattered the pickup H^+. This behavior change may be attributed to a modification in the growth rate sign caused by the presence of oxygen ions, resulting in a damping effect on the PCWs. In addition, the Fourier-transformed dispersion relation of run 1 exhibits a stronger asymmetry between forward-propagating and backward-propagating unstable waves due to the introduction of asymmetry into our system by oxygen particles with pitch angles of ≠90°. Thus, the injected power displays a more plateau-like distribution in the frequency domain, rather than a sharp peak. In this way, we suggest that the free energy brought by newly formed PUIs is converted to the energy of the magnetic field fluctuations, contributing to the plateau-like spectrum. By slightly adjusting the density ratios between pickup O^+ and H^+, we find that the pitch-angle scattering of both ions is slightly modified due to the growth of waves. To test the sensitivity of the initial pitch angle of the PUIs, we also change the pitch angle of pickup H^+ from 30° to 15° while retaining the other parameters similar to run 2. We find that the pickup H^+ are pitch-angle-scattered to around 30° at $t = 120\Omega_{\rm ci}^{-1}$, which is slightly closer to the observation shown in Figure 3(b) (not shown). Indeed, the initial pickup angle also modifies the growth rate of ion cyclotron waves and the subsequent pitch-angle-scattering process as suggested by Cowee & Gary (2012).

4. Discussion and Conclusions

We present a detailed analysis of the formation of a plateau-like magnetic field turbulence spectrum in the magnetosheath of Mars, based on a typical case study and a statistical study observed by MAVEN. For the case study, we reveal that the magnetic field spectrum exhibits flattened $f^{-0.31}$ spectral scaling over the frequency range of 0.01–0.2 Hz, coinciding with the continuous presence of PCWs. This plateau-like spectral feature and the accompanying PUI properties align with our previous statistical result (Jiang et al. 2023), which shows an average occurrence rate of the plateau-like feature of 56% and almost 70% at a pickup angle of around 30°.

Our current analysis further reveals that the formation of the plateau-like spectrum is influenced by the variability of energy injection from PCWs excited by PUI instabilities at Mars. Despite nearly identical background parameters, we observe a 32% decrease in the amplitude of PCWs as the ratio of PUIs $n_{\mathrm{PUI,O}}/n_{\mathrm{PUI,H}}$ increases from 0.01 to 0.58. Additionally, based on 2060 magnetosheath cases resembling plateau-like spectral features in the magnetic field PSD, our statistical result further suggests that the average plateau spectral indices decrease from -0.58 to -0.67 as the ratio $n_{\mathrm{PUI,O}}/n_{\mathrm{PUI,H}}$ increases from 0.002 to 0.56. This finding suggests that the inclusion of pickup O^+ modulates the level of PCWs and consequently alters the flatness of the plateau observed in the magnetic field spectrum. We propose that this modulation arises from the suppression of H^+-driven PCWs by pickup O^+. Furthermore, we provide evidence from in situ observations and numerical simulations utilizing 1D-3V particle-in-cell simulations. Through this combined approach, we establish a possible connection between pickup O^+ and the formation of the plateau-like magnetic field spectrum in the Martian magnetosheath. However, we recognize that the measurement of PUIs is somewhat underestimated due to the field of view of the instrument as well as contamination from thermal ions of solar wind origin. A more accurate estimate should involve comprehensive coverage of the PUIs, considering both energy and angle perspectives, possibly through innovative instrument designs or complementary measurements. For example, this could be partly achieved by combining SWIA, STATIC, and SEP measurements from MAVEN.

We present direct observational evidence of ring-beam-like distributions of pickup O^+ and pickup H^+ in the velocity space. We propose that persistent excitation of PCWs originates from the unstable ring-beam VDF of pickup H^+. The inclusion of pickup O^+ then suppresses the growth rate of PCWs generated by the ring-beam instability of pickup H^+, resulting in a decrease in magnetic field energy injection from pickup H^+. Through pitch-angle scattering, the pickup H^+ ions evolve into bispherical shell velocity distributions (Cowee et al. 2008; Cowee & Gary 2012; Matteini et al. 2015). Our simulations also demonstrate a similar evolution of pickup O^+ toward bispherical shell distributions resembling velocity-space characteristics of pickup O^+ in our observations. As the instability progresses, the magnetic field energy spectrum assumes a more plateau-like shape, eventually reaching a state of nonlinear saturation.

Our simulation results support our hypothesis regarding the observed formation of plateau-like spectra. However, several challenges remain in understanding the key parameters that control the nonlinear evolution of PCWs excited and modulated by multiple species of PUIs, as well as the impact of the plateau-like energy spectrum on background turbulence. The interplay between the nonlinear evolution of waves and background turbulent fluctuations, including the potential existence of an inverse cascade process, remains challenging and requires further quantitative investigations. Our study offers novel insights into the role of kinetic instabilities generated by PUIs in modifying the characteristics of turbulence in the Martian magnetosheath. These findings may also contribute to a better understanding of turbulence in other space plasma environments where significant PUIs are present, such as the outer heliosphere.

Acknowledgments

We thank the entire MAVEN team for providing the data. Data access and processing were done using SPEDAS; see Angelopoulos et al. (2019). The MAVEN spacecraft data used in this study are publicly available through the Planetary Data System: https://doi.org/10.17189/1414251 for MAG, https://doi.org/10.17189/1414229 for SWIA, and https://doi.org/10.17189/1517746 for STATIC. This work is supported by NNSFC grants (grant Nos. 42022032, 42374198, 42188101, 41874203), project of Civil Aerospace "13th Five Year Plan" Preliminary Research in Space Science (D020301). H.L. is also supported by the International Partnership Program of CAS (grant No. 183311KYSB20200017), the National Key R&D program of China No. 2021YFA0718600 and the Chinese-Italian cooperative research project (No. Z221100002722006). H.L. and W.J. are supported by the Specialized Research Fund for State Key Laboratories of China. D.V. is supported by STFC Consolidated grant ST/W001004/1.

Appendix
Method to Extract PUI Density Ratios from SWIA Observation

Since the solar wind ions usually concentrate at limited and fixed look directions in the SWIA's field of view, it is possible to exclude these ions from pickup H^+ by checking the ion differential energy flux spectrograms for each look direction. This method has been proven useful in Rahmati et al. (2017), where they exclude solar wind ions by separating look directions. Although the magnetosheath ions tend to be hotter than the pristine solar wind ions, they are still useful for separating pickup H^+ from the shocked solar wind ions. Figure 6 provides valuable information on the observed ion differential energy flux spectrograms at each look direction from all 64 look directions of SWIA coarse mode. We identify the solar wind ion flux as the most significant ion fluxes coming from azimuths/anodes 14–16 and elevations 1–4. However, from the remaining look directions, we can still observe sufficient ion fluxes with energies close to or slightly greater than the solar wind thermal ions, which we identify as the majority of pickup H^+. For pickup O^+, due to their significantly greater energy than pickup H^+, we can simply keep all ion fluxes with energy above 4000 eV from all look directions and use them as a reasonable approximation of the pickup O^+ flux. Therefore, we combine the pickup H^+ flux with the O^+ flux, shown in the bottom of Figure 6.

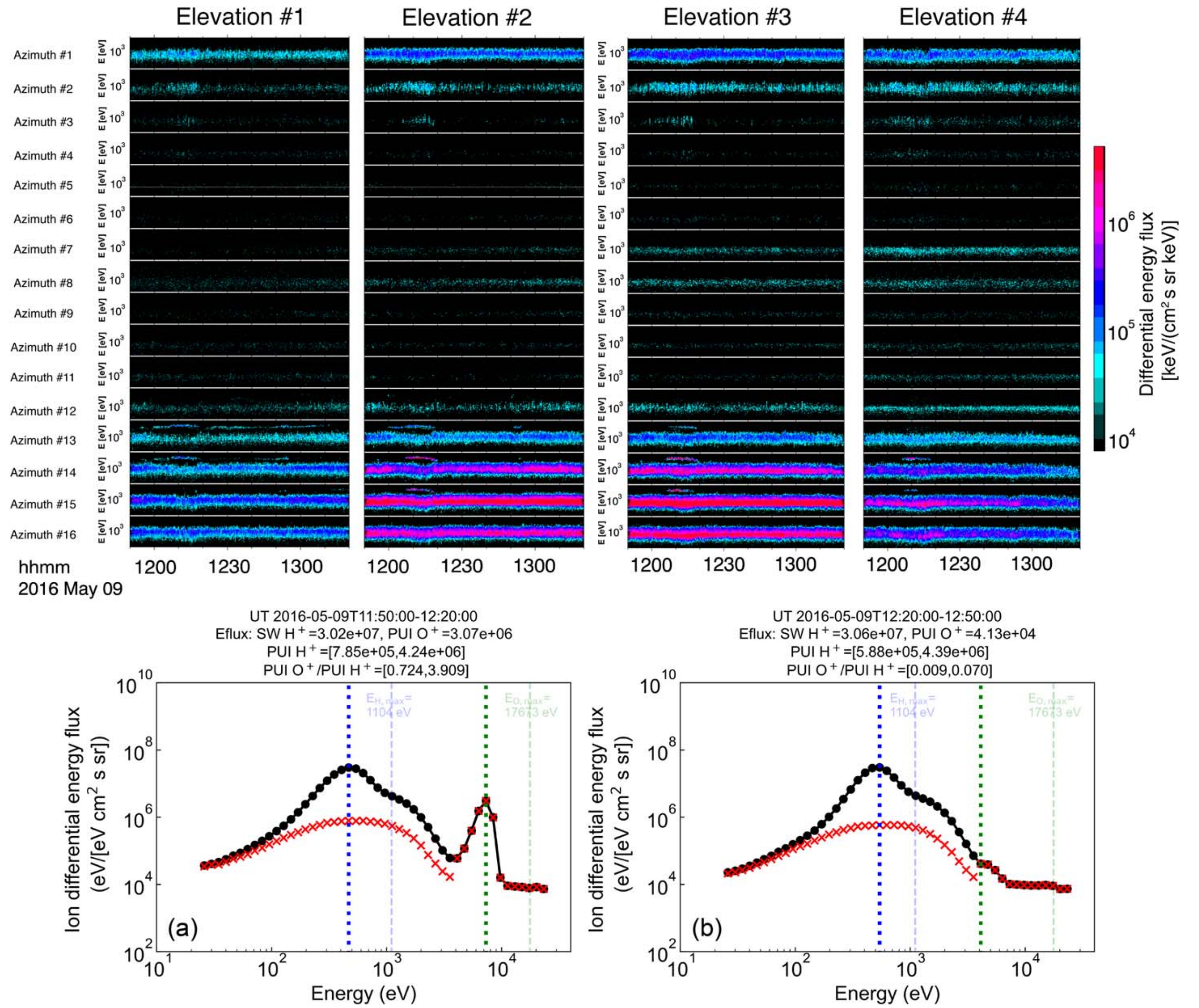

Figure 6. Upper panels: ion energy spectrograms from every single SWIA look direction. SWIA has four elevation channels (displayed horizontally) and 16 anodes (displayed vertically). Lower panels (a) and (b): one-dimensional ion differential energy flux as a function of ion energy from SWIA coarse data for intervals 1 and 2. The black circles represent the ion differential energy flux from all of the look directions of SWIA. The red crosses represent the ion differential energy flux from selected look directions of SWIA (with azimuth 13–16 and elevation 1–4 excluded). The green (blue) vertical dotted lines represent the maximum fluxes of oxygen (hydrogen) PUIs.

In Figures 6(a) and (b), we average the ion differential energy fluxes from all (selective) look directions and show the one-dimensional differential energy flux of all ions (PUIs) in black circles (red crosses) as a function of the ion energy. We compute the upper and lower thresholds for the pickup H^+ at its maximum flux and the flux at its maximum pickup energy $E_{\mathrm{H,max}}$. For pickup O^+, we use the maximum flux above 4000 eV to estimate its flux. For solar wind H^+, we use the maximum flux of ions near the bulk velocity. Consequently, we can estimate the ratios of the differential energy flux of three ion populations. To calculate density ratios, we have to take into account the mass difference between O^+ and H^+, since SWIA overestimates the velocity of O^+ by a factor of $\sqrt{m_{\mathrm{O}}/m_{\mathrm{H}}} = 4$. Therefore, we reduce the flux ratio between O^+ and H^+ by a factor of 4 when converting to a number density ratio. We obtain the density ratios $n_{\mathrm{PUI,O}}/n_{\mathrm{PUI,H}} = [0.18,\ 0.98]$, $n_{\mathrm{PUI,H}}/n_{\mathrm{SW,H}} = [0.03,\ 0.14]$ for interval 1 and $n_{\mathrm{PUI,O}}/n_{\mathrm{PUI,H}} = [0.003,\ 0.02]$, $n_{\mathrm{PUI,H}}/n_{\mathrm{SW,H}} = [0.02,\ 0.14]$ for interval 2. Finally, we take the average ratios of the upper and lower thresholds and obtain $n_{\mathrm{PUI,O}}/n_{\mathrm{PUI,H}} = 0.58$, $n_{\mathrm{PUI,H}}/n_{\mathrm{SW,H}} = 0.08$ for interval 1 and $n_{\mathrm{PUI,O}}/n_{\mathrm{PUI,H}} = 0.01$, $n_{\mathrm{PUI,H}}/n_{\mathrm{SW,H}} = 0.08$ for interval 2 as the input parameters for our simulations.

To confirm our estimate of the density ratios between the three ion populations using ion differential fluxes, we also use the partial moment integration method to obtain the number density of each population and their ratios. Using the same philosophy as the previous method, we distinguish the three ion populations using both look direction and energy. However, we directly integrate the distribution functions for different look directions and energies to obtain partial densities. Figure 7

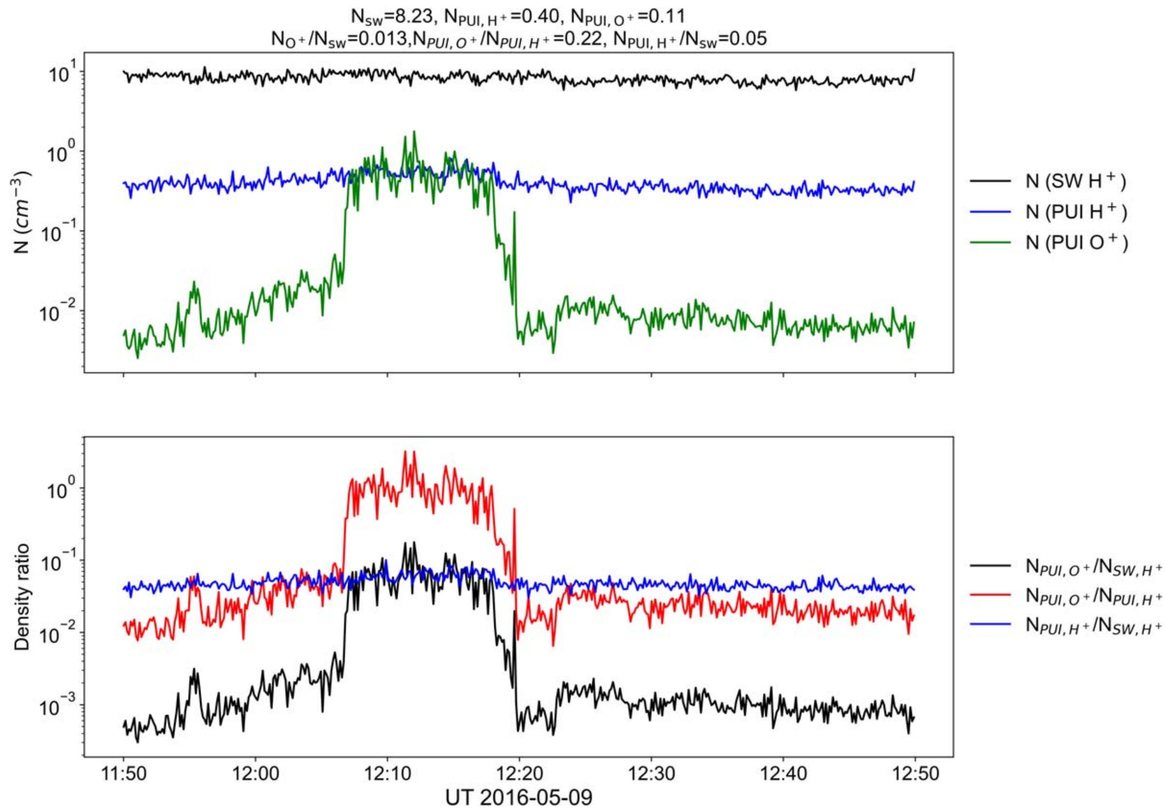

Figure 7. Upper panel: ion number densities of the solar wind H^+ (black), pickup H^+ (blue), and pickup O^+ (green) calculated by the partial moment integration method. Lower panel: density ratios between the pickup O^+ and the solar wind H^+ (black), the pickup O^+ and the pickup H^+ (red), and the pickup H^+ and the solar wind H^+ (blue).

shows the number densities of the solar wind H^+ (black), pickup H^+ (blue), and pickup O^+ (green) calculated by the partial moment integration method. For solar wind H^+, we use ion energy differential flux with energy below 4000 eV and look directions fixed within azimuths 13–16 and elevations 1–4. For pickup H^+, we use data from the remaining look directions with energy below 4000 eV. For pickup O^+, we use data from all look directions with energy above 4000 eV. The lower panel in Figure 7 shows the density ratios between three populations, which are very close to our previous estimates. Therefore, we conclude that the density ratios extracted from SWIA data are reliable.

ORCID iDs

Hui Li https://orcid.org/0000-0002-4839-4614
Wence Jiang https://orcid.org/0000-0001-7431-5759
Zhongwei Yang https://orcid.org/0000-0002-1509-1529
Daniel Verscharen https://orcid.org/0000-0002-0497-1096
Chi Wang https://orcid.org/0000-0001-6991-9398

References

Alexandrova, O. 2008, NPGeo, 15, 95
Andrés, N., Romanelli, N., Hadid, L. Z., et al. 2020, ApJ, 902, 134
Andrés, N., Sahraoui, F., Galtier, S., et al. 2019, PhRvL, 123, 245101
Angelopoulos, V., Cruce, P., Drozdov, A., et al. 2019, SSRv, 215, 9
Brain, D. A. 2002, JGRA, 107, 1076
Bruno, R., & Carbone, V. 2013, LRSP, 10, 2
Chamberlain, J. W. 1963, P&SS, 11, 901
Chasapis, A., Matthaeus, W. H., Parashar, T. N., et al. 2018, ApJL, 856, L19
Chassefière, E., & Leblanc, F. 2004, P&SS, 52, 1039
Connerney, J. E. P., Espley, J., Lawton, P., et al. 2015, SSRv, 195, 257
Cowee, M. M., & Gary, S. P. 2012, JGRA, 117, A06215
Cowee, M. M., Russell, C. T., & Strangeway, R. J. 2008, JGRA, 113, A08220
Cowee, M. M., Winske, D., Russell, C. T., & Strangeway, R. J. 2007, GeoRL, 34, L02113
Cravens, T. E., Kozyra, J. U., Nagy, A. F., Gombosi, T. I., & Kurtz, M. 1987, JGR, 92, 7341
Czaykowska, A., Bauer, T. M., Treumann, R. A., & Baumjohann, W. 2001, AnGeo, 19, 275
Delva, M., Bertucci, C., Volwerk, M., et al. 2015, JGRA, 120, 344
Dong, Y., Fang, X., Brain, D. A., et al. 2015, GeoRL, 42, 8942
Dwivedi, N. K., Schmid, D., Narita, Y., et al. 2015, EP&S, 67, 137
Gary, S. 1991, SSRv, 56, 373
Gary, S. P., & Madland, C. D. 1988, JGR, 93, 235
Hadid, L. Z., Sahraoui, F., Galtier, S., & Huang, S. Y. 2018, PhRvL, 120, 055102
Hadid, L. Z., Sahraoui, F., Kiyani, K. H., et al. 2015, ApJL, 813, L29
Halekas, J. S., Taylor, E. R., Dalton, G., et al. 2015, SSRv, 195, 125
Harada, Y., Ruhunusiri, S., Halekas, J. S., et al. 2019, JGRA, 124, 8707
Hou, C., He, J., Duan, D., et al. 2023, ApJ, 946, 13
Howes, G. G. 2016, ApJL, 827, L28
Huang, S. Y., Hadid, L. Z., Sahraoui, F., Yuan, Z. G., & Deng, X. H. 2017, ApJL, 836, L10
Huang, S. Y., Sahraoui, F., Yuan, Z. G., et al. 2017, ApJL, 836, L27
Huang, S. Y., Wang, Q. Y., Sahraoui, F., et al. 2020, ApJ, 891, 159
Huddleston, D. E., Strangeway, R. J., Blanco-Cano, X., et al. 1999, JGRA, 104, 17479
Jakosky, B. M., Grebowsky, J. M., Luhmann, J. G., & Brain, D. A. 2015a, GeoRL, 42, 8791
Jakosky, B. M., Lin, R. P., Grebowsky, J. M., et al. 2015b, SSRv, 195, 3
Jakosky, B. M., Pepin, R. O., Johnson, R. E., & Fox, J. L. 1994, Icar, 111, 271
Jian, L. K., Russell, C. T., Luhmann, J. G., et al. 2010, JGRA, 115, A12115
Jiang, W., Li, H., Liu, X., Verscharen, D., & Wang, C. 2023, JGRA, 128, e2022JA030874
Jiang, W., Verscharen, D., Jeong, S.-Y., et al. 2024, ApJ, 960, 30
Jiang, W., Verscharen, D., Li, H., Wang, C., & Klein, K. G. 2022, ApJ, 935, 169
Li, H., Jiang, W., Wang, C., et al. 2020, ApJL, 898, L43
Lion, S., Alexandrova, O., & Zaslavsky, A. 2016, ApJ, 824, 47

Matteini, L., Schwartz, S., & Hellinger, P. 2015, P&SS, 119, 3
Neugebauer, M. 1989, JGR, 94, 5227
Osman, K. T., Matthaeus, W. H., Greco, A., & Servidio, S. 2011, ApJL, 727, L11
Rahmati, A., Larson, D. E., Cravens, T. E., et al. 2015, GeoRL, 42, 8870
Rahmati, A., Larson, D. E., Cravens, T. E., et al. 2017, JGRA, 122, 3689
Romanelli, N., Bertucci, C., Gómez, D., Mazelle, C., & Delva, M. 2013, P&SS, 76, 1
Romanelli, N., Mazelle, C., Chaufray, J. Y., et al. 2016, JGRA, 121, 113
Ruhunusiri, S., Halekas, J. S., Espley, J. R., et al. 2017, JGRA, 122, 656
Russell, C. T., Huddleston, D. E., Strangeway, R. J., et al. 1999, JGRA, 104, 17471
Sahraoui, F., Belmont, G., Rezeau, L., et al. 2006, PhRvL, 96, 075002
Sahraoui, F., Hadid, L., & Huang, S. 2020, RvMPP, 4, 4
Santolík, O., Parrot, M., & Lefeuvre, F. 2003, RaSc, 38, 1010
Sonnerup, B. U. Ö, & Scheible, M. 1998, ISSIR, 1, 185
Terres, M., & Li, G. 2022, ApJ, 924, 53
Trotignon, J., Mazelle, C., Bertucci, C., & Acuña, M. 2006, P&SS, 54, 357
Tu, C. Y., & Marsch, E. 1995, SSRv, 73, 1
Verscharen, D., Klein, K. G., & Maruca, B. A. 2019, LRSP, 16, 5
Vörös, Z., Zhang, T. L., Leaner, M. P., et al. 2008, JGRE, 113, E00B21